

Implications of Coronal Line Emission in NGC 4696 *

M. Chatzikos^{1†}, R. J. R. Williams², G. J. Ferland¹, R. E. A. Canning^{3,4},
A. C. Fabian⁵, J. S. Sanders⁶, P. A. M. van Hoof⁷, R. M. Johnstone⁵,
M. Lykins¹, and R. L. Porter⁸

¹Department of Physics & Astronomy, University of Kentucky, Lexington, KY 40506, USA

²AWE plc, Aldermaston, Reading RG7 4PR

³Kavli Institute for Particle Astrophysics and Cosmology (KIPAC), Stanford University, 452 Lomita Mall, Stanford, CA 94305-4085, USA

⁴Department of Physics, Stanford University, 452 Lomita Mall, Stanford, CA 94305-4085, USA

⁵Institute of Astronomy, University of Cambridge, Madingley Road, Cambridge CB3 0HA

⁶Max-Planck-Institut für extraterrestrische Physik (MPE), Giessenbachstrasse, D-85748 Garching, Germany

⁷Royal Observatory of Belgium, Ringlaan 3, 1180 Brussels, Belgium

⁸Department of Physics and Astronomy and Center for Simulation Physics, University of Georgia, USA

Received

ABSTRACT

We announce a new facility in the spectral code CLOUDY that enables tracking the evolution of a cooling parcel of gas with time. For gas cooling from temperatures relevant to galaxy clusters, earlier calculations estimated the $[\text{Fe XIV}] \lambda 5303 / [\text{Fe X}] \lambda 6375$ luminosity ratio, a critical diagnostic of a cooling plasma, to slightly less than unity. By contrast, our calculations predict a ratio ~ 3 . We revisit recent optical coronal line observations along the X-ray cool arc around NGC 4696 by Canning et al. (2011), which detected $[\text{Fe X}] \lambda 6375$, but not $[\text{Fe XIV}] \lambda 5303$. We show that these observations are not consistent with predictions of cooling flow models. Differential extinction could in principle account for the observations, but it requires extinction levels ($A_V > 3.625$) incompatible with previous observations. The non-detection of $[\text{Fe XIV}]$ implies a temperature ceiling of 2.1 million K. Assuming cylindrical geometry and transonic turbulent pressure support, we estimate the gas mass at ~ 1 million M_\odot . The coronal gas is cooling isochorically. We propose that the coronal gas has not condensed out of the intracluster medium, but instead is the conductive or mixing interface between the X-ray plume and the optical filaments. We present a number of emission lines that may be pursued to test this hypothesis and constrain the amount of intermediate temperature gas in the system.

Key words: galaxies: clusters: general – galaxies: clusters: individual: Centaurus – galaxies: individual: NGC 4696 – intergalactic medium – cooling flows – methods: numerical

1 INTRODUCTION

The X-ray-emitting hot intracluster medium (ICM) at the centres of cool core clusters of galaxies can have cooling times shorter than a Hubble time (see, e.g., Fabian 2012). Heating, most likely from active galactic nuclei (AGN) feedback, prevents catastrophic cooling. However, the brightest cluster galaxies in these systems are observed to have substantial quantities of cool and cold gas and star formation relative to their non-cool core analogues and it is widely believed that some residual cooling must occur.

If gas is cooling radiatively then observations of intermediate temperature gas could probe the cooling rates in these systems. Sanders et al. (2008) reported a temperature floor of ~ 4 million K in their dispersive X-ray spectra of the Centaurus cluster. The detection of O VII at much lower levels than predicted by cool-

ing flow models (Sanders & Fabian 2011) indicates that a dearth of 1–3 million K gas is common among cool clusters. If cooling at cluster centres is not impeded by heating mechanisms, it may proceed non-radiatively, e.g., through mixing.

Recently, Canning et al. (2011, C11a) reported a detection of $[\text{Fe X}]$ coronal line emission in NGC 4696, the brightest cluster galaxy in the nearby ($z = 0.0104$, 44.3 Mpc) Centaurus cluster. This line is sensitive to \sim million K gas. If the emission arises from cooling gas, their detection implies a high mass deposition rate of $\sim 20 M_\odot \text{ yr}^{-1}$. However, they do not detect the higher excitation line of $[\text{Fe XIV}]$.

This paper builds upon advances in the spectral simulation code CLOUDY, which permit simulations where the ionization is not in equilibrium with the local gas kinetic temperature (Chatzikos et al., in prep.). Lykins et al. (2013) describe the improvements in the atomic physics which underlies such simulations.

The outline of the paper is as follows. In Sec. 2 we present a brief overview of our numerical implementation of non-equilibrium

* Contains material © British Crown copyright 2011/MoD

† E-mail: mchatzikos@gmail.com

cooling. In Sec. 3 we present modern calculations of the cooling efficiencies for the emission lines pursued by C11a, and emphasize the improvements since Graney & Sarazin (1990, GS90). In Sec. 4 we establish that [Fe X] is optically thin. In Sec. 5 we update the mass deposition rate through [Fe X], and compare it to the mass deposition rate through the X-rays of Sanders et al. (2008). In Sec. 6 we use our CLOUDY simulations to rule out the possibility that the coronal line gas is a cooling condensation of the ambient ICM. Then, in Sec. 7 we use the non-detection of [Fe XIV] to constrain the temperature structure of the coronal gas, and in Sec. 8 we obtain its basic properties based on the detected [Fe X]. We discuss our results in Sec. 9, and summarize in Sec. 10.

2 SPECTRAL SIMULATIONS

This section outlines how we compute the spectrum of a cooling non-equilibrium parcel of gas. The calculations presented here were performed with version r9230 on the “dyna” development branch of the spectral synthesis code CLOUDY (Ferland et al. 2013).

In all cases we begin with a hot gas in collisional ionization equilibrium (CIE) at a preset temperature. We then allow the gas to freely cool, solving for the gas kinetic temperature, the non-equilibrium distribution of ionization (NEI), the gas cooling, and its spectrum.

The implementation of time-dependent physics within CLOUDY is discussed in detail in a separate paper (Chatzikos et al., in prep.). Briefly, our approach builds upon the infrastructure developed by Henney et al. (2005) to treat the structure of steady-state ionization fronts. In its normal mode of usage, CLOUDY uses a hierarchy of solvers to treat the coupled non-linear systems of ionization and level balance, electron density, chemical equilibrium, temperature equilibrium and (where appropriate) pressure equilibrium. By including appropriate source and sink terms in each of these equilibrium solvers, we showed that they could also be used to implement an implicit form of advance from an initial state. In our previous work this initial state was upstream in the flow; in the present case, it is that at the previous time-step.

The time-dependent ionization balance equations may be written as

$$\frac{dn_i}{dt} = \sum_j R_{ji}n_j - R_{ij}n_i. \quad (1)$$

In the standard solver, the terms on the left hand side of this expression are assumed to be zero. In our time-dependent approach, we discretize over time-steps m and time-steps Δt , and use an implicit time-step advance for stability as the full balance system is very stiff. The discretized equations for the state n_i^{m+1} at time-step $m+1$ are then

$$\frac{n_i^{m+1} - n_i^m}{\Delta t} = \sum_j R_{ji}n_j^{m+1} - R_{ij}n_i^{m+1}, \quad (2)$$

where the first term on the left hand side is treated as an additional sink term in the balance matrix.

This approach differs from that used by Gnat & Sternberg (2007), which was based on the database of rates included in a version of CLOUDY that dated from 2006. These authors integrated the ionization rates using a separate ODE solver package, and called CLOUDY directly only to update the cooling rate of the plasma based on the current ionization fractions. The approach which we have adopted allows us to be fully self-consistent in all the components of the time-step advance, and allows the implicit equations

for the advanced state of the system to be solved in discrete physical components, rather than requiring a linear system to be solved for all states of all species in parallel. However, the constraints of working around the existing code have meant that it is at present only possible to use a first-order method for the time advance, so shorter time-steps are required to maintain the accuracy of the solution.

The implementation permits the temporal integration of line emissivities. These are shown to be related to line emission in the classical cooling flow model. In particular, cumulative density-weighted line emissivities¹ are by definition equal to the total line emission in a multi-temperature cooling flow,

$$\begin{aligned} F'_{\text{line}} &= \int dt' j_{\text{line}}(T')/\rho \\ &= \frac{\alpha}{2} \frac{k_B}{\mu m_p} \int_T^{T_{\text{max}}} \frac{\Lambda_{\text{line}}(T')}{\Lambda(T')} dT' \\ &= \Gamma(T, T_{\text{max}}), \end{aligned} \quad (3)$$

where $\alpha = 5$ or 3 , for isobaric (constant pressure, CP) or isochoric (constant density, CD) cooling, respectively, and the mean molecular weight, μ , is a slow function of temperature. $\Lambda_{\text{line}}(T)$ is the frequency-integrated line cooling efficiency, while $\Lambda(T)$ is the cooling function. The integral extends over the temperature range where $j_{\text{line}}(T)$ is finite, but it is customary to extend the range from 0 K to the highest temperature in the gas (and drop the zero from the notation for Γ). Then, $\Gamma(T_{\text{max}})$ encapsulates the total line emission per unit mass of the multi-temperature cooling gas, and determines the line luminosity through

$$L_{\text{line}} = \dot{M} \Gamma(T_{\text{max}}), \quad (4)$$

where \dot{M} is the mass deposition rate (e.g., Sarazin & Graney 1991). The remaining symbols have their usual meaning.

The previous equation was effected by employing the differential cooling time,

$$dt = \frac{\alpha}{2} \frac{n_{\text{tot}} k_B dT}{n_e n_H \Lambda(T)}. \quad (5)$$

Notice that the temporal integration weighs against phases near the peak of the cooling function.

In addition, unweighted cumulative line emissivities² may be computed as

$$\begin{aligned} F_{\text{line}} &= \int dt j_{\text{line}}(T) \\ &= \frac{\alpha}{2} \int_0^{T_{\text{max}}} \frac{k_B \rho}{\mu m_p} \frac{\Lambda_{\text{line}}(T)}{\Lambda(T)} dT. \end{aligned} \quad (6)$$

For isochoric cooling the cumulative integral becomes

$$F_{\text{line}} = \rho \Gamma(T_{\text{max}}), \quad (7)$$

while for isobaric cooling it becomes

$$F_{\text{line}} = \frac{5P}{2} \int_0^{T_{\text{max}}} \frac{\Lambda_{\text{line}}(T)}{\Lambda(T)} \frac{dT}{T}. \quad (8)$$

If the line emits over a restricted range, the temperature may be taken out of the integral as constant, and eqn. (7) is recovered. However, some lines, such as N v $\lambda 1243$ (see below), are prominent over a wide range of temperatures and the inverse temperature dependence in the integral must be retained.

¹ Enabled with the command **set cumulative mass**.

² Enabled with the command **set cumulative flux**.

Table 1. C11a optical coronal lines in Centaurus. The first two columns give the spectroscopic label and wavelength, while the third presents the upper limits relative to the [Fe x] $\lambda 6375$ flux.

Spectral Label	λ / Å	Flux Ratio
[Fe xiv]	5303	<1.29
[Ca xv]	5445	<0.29
[Ca xv]	5695	<1.09
[Ni xv]	6700	<0.31

3 COMPARISON WITH PREVIOUS CALCULATIONS

The numerical advances and the atomic data updates (Lykins et al. 2013) will cause significant changes from the predictions in the seminal paper of GS90. The recombination rates are now significantly larger due to the incorporation of recombination channels which were not known twenty years ago. The atomic line database used to compute the cooling is far larger than was available previously, due to our use of both Opacity Project and Chianti line data. Even for lines in common with Sarazin & Graney (1991), the cooling can be quite different due to our use of high-quality close coupling collision rates, rather than the simpler rates that were available at that time.

Table 1 lists the optical coronal lines of interest. To facilitate a direct comparison to the GS90 predictions for these lines, we have computed their emissivity for a unit volume of gas, as it cools from 8×10^7 K, appropriate to the ICM, to 10^5 K, adopting the same abundances (Meyer 1979).

Figure 1 illustrates the comparison between the emission coefficients reported by GS90 and the present calculations. The most evident difference is a general shift to lower temperatures. The calcium lines are suppressed by $\sim 1\text{--}2$ dex above 8×10^6 K. The [Fe x] $\lambda 6375$ line is shifted to a maximum around a million K, leading to 1 dex of suppression at higher temperatures, and a comparable boost at lower temperatures. The cooling efficiency of [Fe xiv] $\lambda 5303$ is also boosted below its former peak, but is roughly unchanged above it. The maximum efficiencies are within a factor of 2 of the GS90 results, except [Ni xv] $\lambda 6700$, which is depressed by ~ 4 .

These remarks are relevant to the C11a observations. The fact that the cooling efficiency of [Fe xiv] $\lambda 5303$ has increased *over the entire temperature range* suggests that its non-detection cannot be due to uncertainties in the atomic data, as they cautioned. Quite the contrary, the enhancement of the emissivity below 2×10^6 K places more stringent limits on the exact temperature range covered by gas, as we discuss below.

4 [Fe x] OPTICAL DEPTH

It is important to estimate the optical depth to [Fe x] through the Centaurus galaxy cluster ICM, and the warm gas of NGC 4696. Figure 2 shows the optical depth due to continuum opacity through a 1 cm slab of gas at unit hydrogen density as a function of temperature. The opacity is dominated by Thomson scattering off of free electrons. Below 20,000 K the main contributor to opacity is continuum absorption.

Because of our choice of unit density, numerically the continuum opacity is roughly equivalent to the extinction cross-section (to within a factor of a few). It follows that the inverse of the opacity amounts to the hydrogen column density required for $\tau \sim 1$. The largest value reported by Crawford et al. (2005) is not higher than

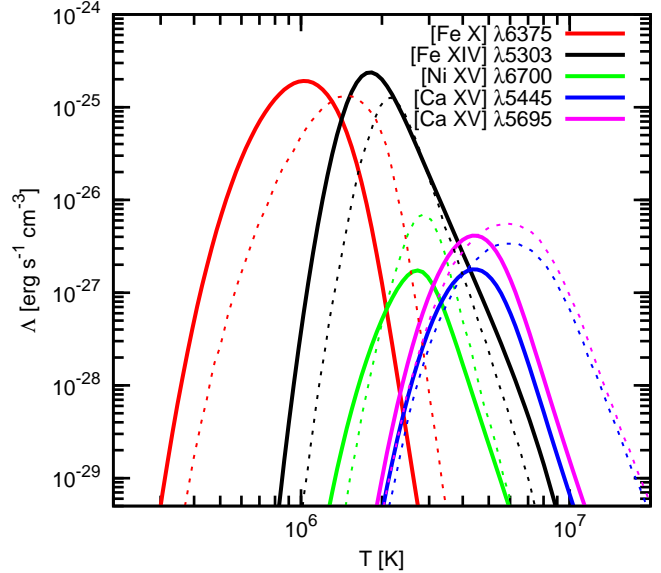


Figure 1. Isochoric cooling efficiency for the lines discussed by C11a. Solid and dotted lines show the present and GS90 results, respectively. The lines as listed in the legend proceed from left to right.

10^{22} cm^{-2} . This indicates that gas hotter than 10,000 K is optically thin to radiation at [Fe x].

Mittal et al. (2011) computed the gas-to-dust ratio through a 7 kpc aperture to be at best 70. O’Dea et al. (1994) estimated the amount of molecular gas to $\sim 5 \times 10^8 M_\odot$ (see Mittal et al.), which we adopt here as the total mass for the molecular and dust components. This translates to a column density of $\sim 2 \times 10^{21} \text{ cm}^{-2}$. Combined with the declining absorption cross-section, we conclude that the cold matter in NGC 4696 is also optically thin to [Fe x].

Finally, extinction due to spectral lines is also negligible, as it is at most five orders of magnitude smaller than the continuum.

5 COMPARISON TO X-RAY GAS

Sanders et al. (2008) modelled their dispersive *XMM-Newton* spectra with cooling flow models and reported that no significant quantities of cool ($\lesssim 0.4$ keV) gas were detected. Comparison with spatially resolved spectra obtained with *Chandra* (Sanders & Fabian 2006) indicates that the lowest temperatures arise from the central $30''$, while higher temperatures are emitted progressively farther from the cluster centre. In fact, their best-fitting cooling flow models were consistent with mass deposition rates that diminish with decreasing temperature. An upper limit of $0.8 M_\odot \text{ yr}^{-1}$ was obtained for their lowest temperature of 0.25 keV. Similar results were obtained from spectral line analysis.

The coronal lines probe temperatures of 1–5 million K, and offer a complementary view into cooling at and beyond the softest bands accessible to X-rays. In order to constrain the state and origin of the coronal line gas, it is important to test whether it is consistent with being due to cooling from a possibly abated cooling flow.

For our analysis, we employ CLOUDY calculations that track a unit volume of gas at a hydrogen density of 0.07 cm^{-3} as it cools from 80 million K to 10,000 K, and ignore the transfer of the optically thin coronal lines. (Our results are not sensitive to the exact density value.) We adopt the abundances for the coolest of the five-

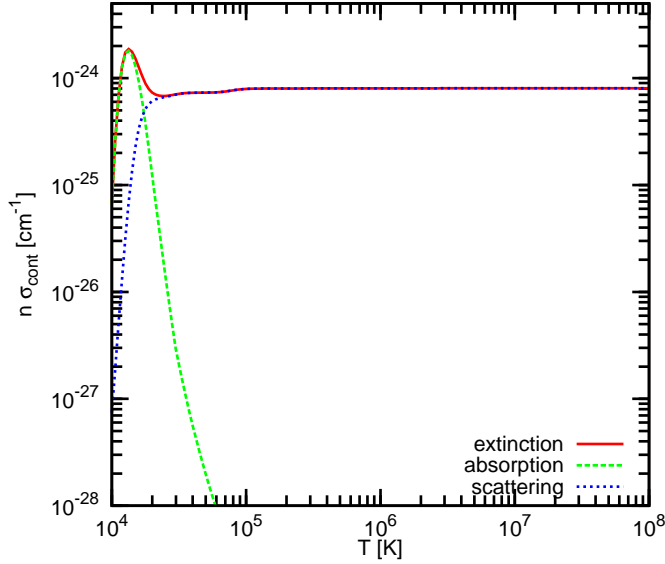


Figure 2. Variation of continuum opacity with temperature for a 1 cm slab of unit hydrogen density. The contributions of absorption and scattering are also presented.

Table 2. Adopted elemental abundances relative to hydrogen in our simulations. The second column lists the solar abundances of Anders & Grevesse (1989). The last two columns list the abundances for the cool gas component obtained in the fits of Sanders et al. (2008): the five-component cooling flow model (third column), and the five-temperature thermal model (last column).

Element	Solar	5×VMCFLOW	5×VAPEC
Nitrogen	1.12E−4	3.93E−4	1.80E−4
Oxygen	8.51E−4	4.43E−4	4.00E−4
Neon	1.23E−5	9.84E−5	9.10E−5
Magnesium	3.80E−5	3.88E−5	3.46E−5
Silicon	3.55E−5	6.24E−5	5.68E−5
Calcium	2.29E−6	6.41E−6	5.96E−6
Iron	4.68E−5	5.05E−5	4.54E−5
Nickel	1.78E−6	4.52E−6	4.16E−6

component cooling flow model of Sanders et al. (2008) as the most appropriate for the question at hand, listed in the third column of Table 2.

Figure 3 illustrates the ionization fractions of the relevant ions for both CIE and NEI isochoric calculations. Isochoric calculations produce identical results and are not shown. Evidently, in this temperature range cooling and recombination are in equilibrium, in agreement with GS90 and Gnat & Sternberg (2007). The ionization fraction of Fe^{6+} is also presented to illustrate that non-equilibrium effects become important at lower temperatures.

We begin by recalculating the mass deposition rate through [Fe X]. C11a reported that the luminosity in [Fe X] is $3.5 \times 10^{37} \text{ erg s}^{-1}$, which translates to $\dot{M} \sim 1.63 M_{\odot} \text{ yr}^{-1}$, given that $\Gamma \approx 3.42 \times 10^{11} \text{ erg g}^{-1}$ for isobaric cooling. (For isochoric cooling, $\Gamma \approx 2.07 \times 10^{11} \text{ erg g}^{-1}$, and the mass rate is $\sim 2.68 M_{\odot} \text{ yr}^{-1}$.) This is significantly lower than the rate of $20 M_{\odot} \text{ yr}^{-1}$, deduced by C11a using the older results of Sarazin & Graney (1991), and in overall agreement with the X-ray spectroscopy results. Note, however,

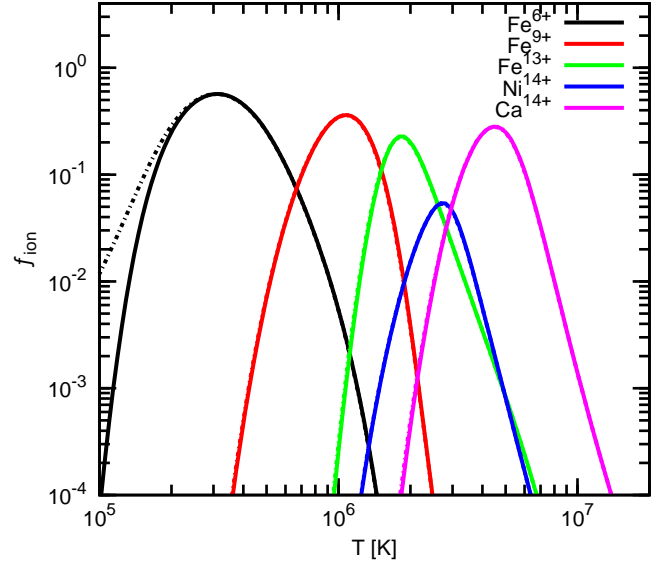


Figure 3. Fractional densities for the ions discussed by C11a, and for Fe^{6+} . Results are presented for both CIE (solid) and NEI (dashed) calculations of isochoric cooling. Recombination lags become significant below $2 \times 10^5 \text{ K}$. The ions as listed in the legend proceed from left to right.

that this estimate is in excess of the upper limit of $0.8 M_{\odot} \text{ yr}^{-1}$ obtained by Sanders et al. (2008) by fitting the entire spectrum with a multi-component cooling flow model.

In Table 3, we investigate the consistency of our cooling calculations against the cooling flow model predictions of Sanders et al. (2008, see Table 3 therein). Following that work, our models cool from an initial temperature of $\sim 4.5 \text{ keV}$. However, we do not employ solar metallicities as in that work, but instead use the abundances appropriate to their five-component VMCFLOW model as before. Note from Table 2 that the iron abundance is close to the solar value, while the nitrogen abundance is 3.5 times higher. We compute the $\Gamma(T)$ functions for these lines, and convert the X-ray luminosities to mass deposition rates with the aid of eqn. (4). Our calculations are in good agreement with the reported rates (shown in the last column of Table 3). N VII is the only exception because the adopted solar abundance in that paper is unrealistically low for the X-ray gas (see Sanders et al. for more details). Adjusting the reported mass deposition rate through N VII by 3.5 leads to a value comparable to the rate calculated by CLOUDY.

Table 4 presents estimates for the mass deposition rate through the [Fe X] coronal line. These are obtained first by converting the ratio of X-ray to coronal luminosities into ratios of the mass deposition rates, and then by invoking the reported mass rates through the X-ray lines. The mass deposition rates cover the range $1\text{--}4 M_{\odot} \text{ yr}^{-1}$, in agreement with our estimate from the coronal line alone.

This analysis indicates that the mass deposition rate through the coronal line is in reasonable agreement with the rates obtained from the X-ray lines. In principle, then, the coronal gas is consistent with cooling out of the hot ICM at a uniform rate in the range $1\text{--}10$ million K. If that were the case, the expected luminosity for [Fe XIV] is about $10^{38} \text{ erg s}^{-1}$, or about twice the upper limit. (This result may be obtained by comparing to Fe XVII $\lambda 15.01$ assuming a uniform deposition rate, and noting that for the coronal line

$\Gamma(T) = 5.9343 \times 10^{11} \text{ erg g}^{-1}$ for isochoric cooling.) The fact that the 2 million K [Fe XIV] line is not observed is perplexing.

6 CORONAL GAS AS A COOLING CONDENSATION

Deciphering the lack of any [Fe XIV] emission is fundamental to our understanding of the state of the coronal gas. If the coronal gas is indeed cooling out of the ambient ICM, the mass deposition rate through [Fe XIV] should be consistent with the X-ray and coronal line rates. We now leverage our cooling models to convert the upper limit to the luminosity ratio to a limit for the ratio of mass deposition rates.

Table 5 lists our estimates for the $\Gamma(T)$ ratio between each of the undetected lines and the detected [Fe X]. They amount to the luminosity ratios expected for a simple cooling flow model of uniform deposition rate. Interestingly, the ratio of $\Gamma(T)$ functions for [Fe XIV] is greater than the observed limit, suggesting that if the coronal gas was cooling freely from the hot ICM, the [Fe XIV] would probably have been observed.

6.1 Continuum Subtraction

The C11a upper limits depend sensitively on the continuum subtraction method employed (see Sec. 3.3 therein). In particular, single stellar population model spectra are dominated by stellar features below 6000 Å, which vary on scales comparable to the expected coronal line widths, complicating the analysis. C11a stress that the uncertainties in the stellar continuum subtraction may introduce a larger error into the reported upper limit for [Fe XIV].

We note that our calculations yield a $\Gamma(T)$ function ratio of 2.85 for [Fe XIV] over [Fe X]. By contrast, the older models of Graney & Sarazin (1990) predict values less than unity. This is a consequence of the changes in the [Fe XIV] $\lambda 5303$ Å emissivity discussed in Sec. 3. In other words, our findings further exacerbate the non-detection of [Fe XIV].

While we acknowledge the complications involved in estimating accurate fluxes for the [Fe XIV] line, in the following, we assume that the non-detection is not due to such technicalities, and explore its consequences for the state of the system.

6.2 Mass Deposition Rates

Accounting for the upper limits of C11a, the $\Gamma(T)$ ratios can be converted to upper limits for the mass deposition rate through

$$\frac{\dot{M}_{\text{line}}}{\dot{M}_{[\text{Fe X}]}} < \frac{L_{\text{line}}}{L_{[\text{Fe X}]}} \frac{\Gamma_{[\text{Fe X}]}}{\Gamma_{\text{line}}}. \quad (9)$$

The maximum rates are presented in Table 6. Our calculations suggest that the mass deposition rate at a million K ([Fe X]) is twice as high as the rate at two million K ([Fe XIV]), or that more gas is cooling from a million K, than is cooling to that temperature. This contradicts cooling flow observations, which suggest that the mass deposition rate is either constant or increases with temperature.

The lack of any significant [Fe XIV] emission suggests that the coronal gas cannot have formed in situ as a cooling condensation of the surrounding ICM. It is more likely that, as the X-ray morphology suggests, the gas originated closer to the galactic nucleus, and it has been displaced to its current position by a dynamical process, such as uplifting by radio bubbles, and possibly heated. Other possibilities, such as conduction and mixing, are discussed in Section 9.

6.3 Differential Extinction

Before we investigate the properties of the coronal gas in more detail, we explore the possibility that the lack of [Fe XIV] emission is due to extinction. Having established that the detected coronal line is optically thin, steep extinction laws are required to account for the observations.

Mittal et al. (2011) reported the detection of extended dust emission in NGC 4696. If the X-ray cool gas resides on the far side of the radio source, extinction may account for the non-detection of [Fe XIV]. Assuming a constant mass deposition rate in the 1–2 million K range, the reddening between [Fe XIV] and [Fe X] is

$$A_{5303} - A_{6375} > -2.5 \log_{10} \left(\frac{L_{[\text{Fe XIV}]}}{L_{[\text{Fe X}]}} \frac{\Gamma_{[\text{Fe X}]}}{\Gamma_{[\text{Fe XIV}]}} \right). \quad (10)$$

Because these wavelengths lie in the linear part of the extinction curve (Fitzpatrick 1999), they are largely independent of the reddening constant, $R = A_V / E(B - V)$, and may be approximated by $A_{5303} - A_{6375} \simeq 0.24 A_V$. For the values shown in Tables 1 and 6, we obtain $A_V > 3.6125$. The detailed dependence of the differential extinction on the V-band extinction is shown in Figure 4. Note that mass deposition rates that decrease with declining temperature, as suggested by X-ray spectroscopy (Sanders et al. 2008), would require even heavier extinction.

The required minimum extinction is difficult to reconcile with observations, as it exceeds the maximum V-band extinction estimates in the vicinity of NGC 4696. Sparks et al. (1989) reported a maximum of 0.4 at the south-western end of the dust lane, based on V- and R-band imaging. On the other hand, Farage et al. (2010) estimated a maximum of ~ 0.7 , 3'' north-west of the nucleus, from the observed $H\alpha/H\beta$ ratio, and the standard assumption for active galaxies that its intrinsic value is higher than the Case B value, at 3.1. Canning et al. (2011) reported maximum extinctions of $A_V \sim 2$ –2.5 (see fig. B1 in their appendix) for a Case B $H\alpha/H\beta$ ratio. For values appropriate to active galaxies, however, they obtained results consistent with Farage et al. (2010). Similar results have been obtained by other authors (e.g., see references in Canning et al. 2011).

In any case, there is not significant overlap between the gas cloud of interest (“box 1” in C11a) and regions of high extinction according to fig. B1 of Canning et al. (2011), although C11a point out that assessing the connection between the coronal line gas, and the optical filaments and dust lane will require deeper observations.

Also note that these conclusions are in qualitative agreement with the modelling of Werner et al. (2013). These authors postulated the presence of intervening cold absorbers intermixed with the X-ray filaments in Virgo, and found that a column density of $1.6 \times 10^{21} \text{ cm}^{-2}$ may account for the lack of X-ray emission below 0.5 keV. If a column density of that magnitude occurs in Centaurus as well, it would translate to reddening $E(B - V) = 0.276$, according to the dust-to-gas relation of Bohlin et al. (1978), namely, $N(\text{H I} + \text{H}_2) = 5 \times 10^{21} E(B - V)$. However, such a column can only account for the preferential extinction of the [Fe XIV], if the reddening constant has a value $R \gtrsim 13$. We can therefore rule out this possibility, as well.

We conclude that extinction cannot account for the lack of [Fe XIV] emission.

6.4 Heating

Heating may prevent a gas from cooling to low temperatures either by establishing a temperature floor, or by increasing the thermal energy of the gas and reducing its net cooling rate. Because the

Table 3. Updated mass deposition rates for the detected X-ray lines of Sanders et al. (2008) based on our isobaric calculations. For a more fair comparison, the integrations are done starting at a temperature of about 4.5 keV. However, we do not assume solar metallicities. Instead, our results are drawn from calculations employing the abundances of their 5×VMCFLOW model (see Table 2). The first two columns identify the X-ray emission line. The third column lists the reported line luminosity. The fourth column lists the $\Gamma(T)$ functions, which are converted to mass deposition rates in the fifth column with the aid of eqn. (4). Finally, the last column shows the reported mass deposition rates for comparison.

Label	$\lambda / \text{\AA}$	$L / 1\text{E}+39 \text{ erg s}^{-1}$	$\Gamma(T) / \text{erg g}^{-1}$	$\dot{M}_{\text{calc}} / M_{\odot} \text{ yr}^{-1}$	$\dot{M}_{\text{rep}} / M_{\odot} \text{ yr}^{-1}$
Fe XVII	15.01	12.4	1.23E+14	1.60	1.6
Fe XVII	15.26	3.6	3.32E+13	1.72	1.6
Fe XVII	16.78	4.3	6.13E+13	1.11	1.7
Fe XVII	17.05	19.3	7.64E+13	4.00	3.0
N VII	24.78	11.5	5.00E+13	3.65	9.7

Table 4. Coronal mass deposition rates based on the detected X-ray lines reported by Sanders et al. (2008). The first two lines identify the X-ray line. The third column lists the ratio of the X-ray luminosity to that of [Fe x] $\lambda 6375$. The fourth column lists the ratio of the $\Gamma(T)$ functions for a freely cooling gas (isochoric and isobaric cooling produce virtually identical ratios). The fifth column lists the ratio of mass deposition rates of the X-ray line relative to that of the coronal line, obtained with eqn. (4). The last column lists the mass deposition rate in the coronal line using the reported X-ray mass deposition rate, listed in the last column of Table 3.

Label	$\lambda / \text{\AA}$	$L/L(\text{Fe x})$	$\Gamma(T)/\Gamma(T)(\text{Fe x})$	$\dot{M}/\dot{M}(\text{Fe x})$	$\dot{M}(\text{Fe x}) / M_{\odot} \text{ yr}^{-1}$
Fe XVII	15.01	354	359	0.99	1.6
Fe XVII	15.26	103	97	1.06	1.5
Fe XVII	16.78	123	180	0.68	2.5
Fe XVII	17.05	551	224	2.46	1.2
N VII	24.78	329	146	2.25	4.3

Table 5. Ratio of gamma functions, $\Gamma_{\text{line}}/\Gamma_{[\text{Fe x}]}$, for cooling calculations of the five-component cooling flow model of Sanders et al. (2008). The first two columns identify the spectral line, while the remaining columns list results for NEI and CIE cooling under isochoric (CD) and isobaric (CP) conditions.

Spectral Line		NEI-CP	CIE-CP	NEI-CD	CIE-CD
Label	$\lambda / \text{\AA}$				
[Fe XIV]	5303	2.84	2.84	2.85	2.87
[Ca XV]	5445	0.24	0.25	0.24	0.25
[Ca XV]	5695	0.56	0.57	0.56	0.58
[Ni XV]	6700	0.07	0.07	0.07	0.07

Table 6. Upper limits to the ratios of mass deposition rates, obtained with the results of Table 5, and eqn. (9). The meaning of the columns is the same as in Table 5.

Spectral Line		NEI-CP	CIE-CP	NEI-CD	CIE-CD
Label	$\lambda / \text{\AA}$				
[Fe XIV]	5303	0.45	0.45	0.45	0.45
[Ca XV]	5445	1.19	1.17	1.20	1.16
[Ca XV]	5695	1.94	1.90	1.96	1.89
[Ni XV]	6700	4.34	4.28	4.38	4.26

details of how heating affects gas at different temperatures are uncertain, simulations of the latter scenario fall beyond the scope of the present paper. In this paper, we assume that heating, if it has occurred, has merely established a temperature floor. If the floor falls in the temperature range probed by [Fe x], it will affect the deduced mass deposition rates.

Figure 5 explores the temperature dependence of the computed gamma ratios, as well as the maximum deposition rate ratios

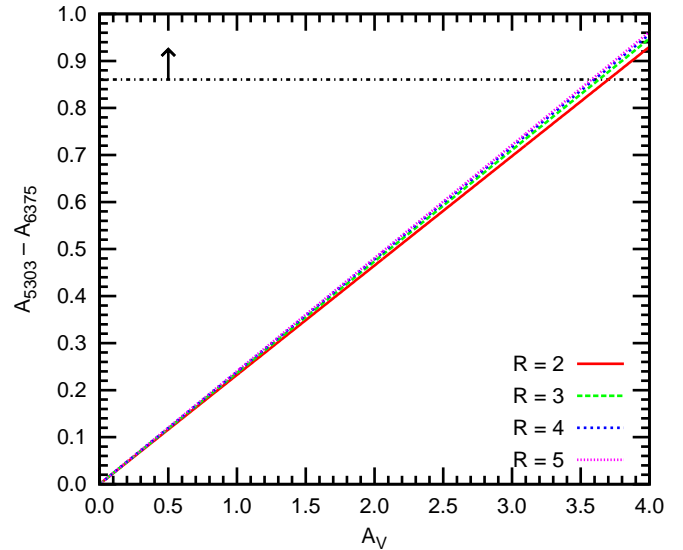


Figure 4. Dependence of differential extinction on the V-band extinction for a number of different R extinction laws. The dot-dashed line shows the limit derived from the observations for a $\Gamma(T)$ ratio of 2.85 (see Table 6).

subject to the observed luminosity upper limits. The $\Gamma(T)$ functions are computed between the initial temperature in the simulation and the temperature floor in question, T . In practice, an emission line contributes significantly over a limited temperature range. The range for the plots is chosen to cover most of the range probed by the [Fe x] line (see Fig. 1). At the left end of these plots, the $\Gamma(T)$ and \dot{M} ratios are near the asymptote values shown in Table 6. At higher temperatures, the amount of cooling due to [Fe x] dimin-

ishes causing the $\Gamma(T)$ ratios to increase, and the mass deposition rate ratios to decrease.

It is important to notice that the $\Gamma(T)$ ratio for [Fe XIV] is always higher than unity, suggesting that cooling due to this line is more important than cooling due to the [Fe X] *over the entire temperature range*. This is partly because the gas cools faster through the temperature range probed by [Fe X].

The right panel of Fig. 5 illustrates that the mass deposition rate consistent with the observed upper limits for [Fe XIV] is *always* lower than the rate traced by [Fe X]. In fact, the rate becomes progressively lower at higher temperatures, as the cooling due to [Fe X] diminishes. If extinction is at work, even higher values than previously computed are required to account for the increasing $\Gamma(T)$ ratios.

These arguments show that a simple temperature floor cannot account for the lack of emission from gas hotter than \sim million K in the observations of C11a, and support our conclusion that the coronal gas cannot be a cooling condensation of the surrounding ICM.

7 CONSTRAINTS FROM [Fe XIV]

As discussed in Section 8, constraining the properties of the coronal gas requires an estimate of the volume it occupies. The coronal gas was detected along the cool X-ray plume (Sanders & Fabian 2002), and most likely it is embedded within the X-ray filament. However, the connection between the X-ray and coronal phases, as well as the optical filaments, remains unclear (C11a).

In this section we consider the possibility that the coronal gas is projected on to the X-ray cool filament by chance, and arrive at an estimate for its volume fraction. For this purpose, we assume that gas cooling may be described by the cooling flow formalism, in the sense that line luminosities are given by eqn. (4). Because cooling is thought to occur “locally”, we take the mass deposition rate to be constant. Differences in the cooling rate are encapsulated in the $\Gamma(T)$ function, and fully accounted for when taking line ratios. We also adopt the abundances of the $5\times$ VAPEC model fits of Sanders et al. (2008), shown in the last column of Table 2. Note, however, that the differences to the abundances appropriate to the five component cooling flow model are within the statistical errors (10%) for most elements.

7.1 Temperature Ceiling

We consider the luminosity ratio between the [Fe XIV] and [Fe X] lines computed over the temperature intervals which contribute 99% of the respective total line luminosity. Our goal is to obtain an estimate for the maximum temperature of the coronal gas that is consistent with the reported upper limit ($[\text{Fe XIV}] / [\text{Fe X}] < 1.29$). We let the maximum temperature of the gas vary between the temperature at which the cooling efficiency of [Fe XIV] peaks (1.8 million K) and the upper end of the line temperature range. We also explore the robustness of these calculations in the presence of a temperature floor, which we simulate by letting the minimum temperature probed by [Fe X] be at most equal to the temperature of peak cooling efficiency (~ 1 million K) and no less than the lower end of the line temperature range. (The temperature range probed by [Fe X] is $T_{\min}^X \leq T \leq T_{\max}^X$.) Figure 6 shows that the computed luminosity ratio is consistent with the reported upper limit for temperatures no greater than 2.1 million K. This is true for both isochoric and isobaric cooling. The presence of a temperature floor

does not modify these results significantly. In the following, we adopt a conservative temperature ceiling of 2.1 million K.

7.2 Volume Filling Factors

The volume occupied by gas in the temperature range $(T, T + dT)$ is $dV = \dot{M} dt / \rho$. For a constant mass deposition rate, the volume of gas in (T_1, T_2) is

$$V = \dot{M} \int_{T_1}^{T_2} dt / \rho = \dot{M} Z(T_1, T_2). \quad (11)$$

The total volume of the cooling gas may be obtained by extending the integral limits to include the entire range of temperatures covered by the gas. Then, the volume fraction for gas over a limited temperature range is given by the ratio

$$f_V = Z(T_1, T_2) / Z(T_{\min}, T_{\max}). \quad (12)$$

We compute the volume fraction of the [Fe X] phase as a function of the temperature floor, which we let extend to 10,000 K. The integration in the numerator of eqn. (12) is carried out over the range (T, T_{\max}^X) , where $T \geq T_{\min}^X$. In the denominator the integration is carried out over (T, T_{\max}) , where T_{\max} is the adopted temperature ceiling. As Figure 7 shows, typical values are in the range of 50–75%. For isobaric cooling, the volume fraction obtains an asymptotic value at low temperatures, due to compression. For isochoric cooling, by contrast, the volume fraction declines with decreasing temperature below 200,000 K. The NEI calculations predict a slightly lower volume fraction. This is due to reduced cooling relative to CIE (Gnat & Sternberg 2007), which leads to gas surviving for longer at such temperatures.

8 CORONAL GAS PROPERTIES

The [Fe X] luminosity may be used to infer the coronal gas properties. Motivated by the optical and X-ray filaments in the same region, we approximate the coronal gas as a cylinder, and take its diameter and height equal to the size reported by C11a, i.e., $2R \sim 700$ pc. Below we first explore the scenario that the coronal gas is independent of the X-ray plume, and then that it is embedded within the plume.

8.1 Independent Structure

We assume that the temperature floor lies below the range of [Fe X] emission, but not by much. This allows us to adopt a volume filling factor of 60%. We accumulate line fluxes according to eqns. (6)–(8), and solve the standard equation

$$L^X = f_V V n_e n_H \Lambda^X(T), \quad (13)$$

for the hydrogen density, n_H . The computed accumulated fluxes are rescaled by the square of the density at the temperature of peak [Fe X] cooling, \sim million K, for that purpose.

All cooling runs are consistent with a hydrogen density of $\sim 0.2 \text{ cm}^{-3}$. This includes isochoric and isobaric calculations, in and out of collisional equilibrium. The obtained density is not sensitive to the adopted volume fraction, $n_H \propto f_V^{-1/2}$, and values in the range 50–75% lead to small density variations. The coronal gas mass is about $1.5 \times 10^6 M_\odot$.

If we assume that the coronal gas is thermally supported, pressure equilibrium translates to a distance of the cloud to the radio

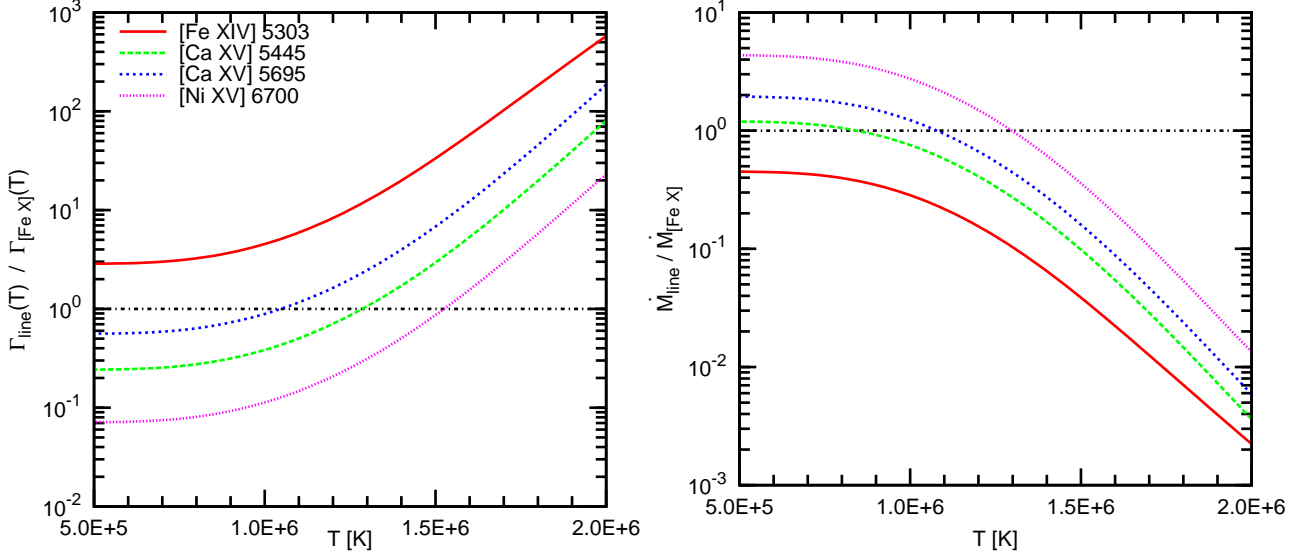


Figure 5. (Left panel) Ratio of $\Gamma(T, T_{\text{max}})$ for each of the non-detected lines against the detected [Fe X], as a function of temperature. (Right panel) Maximum deposition mass rates for each of these lines, computed as the r.h.s. of eqn. (9), as a function of temperature.

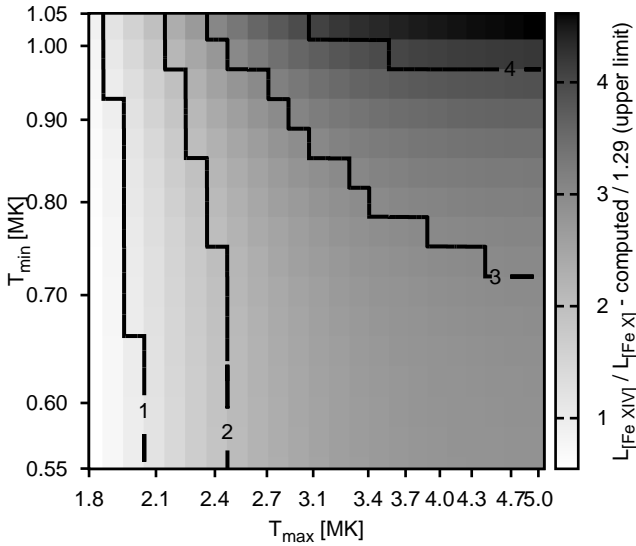


Figure 6. Ratio of the computed luminosity ratio of [Fe XIV] over [Fe X] in units of the reported upper limit (1.29). The results shown are for isobaric cooling. The temperature ceiling varies along the x-axis, while the temperature floor varies along the y-axis. The upper limit is consistent with a temperature ceiling of ~ 2.1 million K.

source of about 20 kpc. However, C11a concluded that the [Fe X] is turbulently broadened at $\sim 300 \text{ km s}^{-1}$. We have therefore assumed that transonic turbulence ($v_{\text{turb}} \sim c_s$, where v_{turb} is the turbulent velocity, and c_s is the sound speed) contributes to the pressure budget of the coronal cloud. This leads to a linewidth of $\sim 250 \text{ km s}^{-1}$, in decent agreement with the observations. Pressure equilibrium, then, translates to a distance of $\sim 8 \text{ kpc}$, suggesting that the X-ray arc is located within NGC 4696. The projected distance from the nucleus is $\sim 3 \text{ kpc}$, so the line-of-sight distance to the nucleus is $\sim 7.5 \text{ kpc}$.

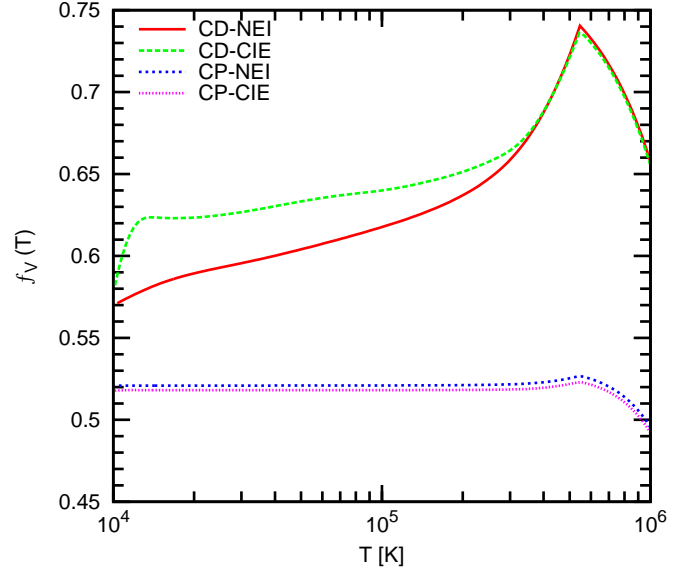


Figure 7. Volume fraction of the phase that emits [Fe X] as a function of the temperature floor. The calculations are done for temperatures below the cooling efficiency peak. The line cooling efficiency effectively drops to zero below 0.55 million K.

The sound crossing time of the coronal cloud is about 4.5 Myr. By contrast, the gas cooling time is $\sim 0.6 \text{ Myr}$ for isochoric cooling, and $\sim 0.8 \text{ Myr}$ for isobaric cooling. In either case, the cooling time is a small fraction of the crossing time, which suggests that the gas cooling proceeds under conditions of constant density (isochoric).

In cooling flow models, the gas is cooling such that its temperature follows the underlying gravitational potential (McNamara & Nulsen 2007). This property allows to test for the possibility that the gas has been displaced to the observed location. An alternative method is to compare the entropy content of the coronal gas to that of the surrounding ICM, as described by the fitting forms

of Graham et al. (2006). Note that the ICM follows the familiar $K(r) \propto r^{0.96}$ entropy law down to ~ 1 kpc from the nucleus. We find that the coronal gas carries about 1/90 of the entropy in the surrounding X-ray gas. If the entropy distribution holds at sub-kpc scales, the coronal gas entropy is consistent with a distance of ~ 0.1 kpc from the nucleus, and therefore consistent with a displacement scenario.

8.2 Embedded In X-ray Plume

If the coronal gas is embedded within the X-ray plume, we can require that it be in pressure equilibrium with the hot phase, and we can use the coronal luminosity to constrain its volume fraction.

The X-ray gas is estimated to have a density of 0.13 cm^{-3} , and a temperature of 0.8 keV (Sanders & Fabian 2002). We assume that the coronal gas covers the range of temperatures probed by [Fe X]. A wider range would introduce a 50-75% correction to its volume fraction, as discussed previously. We also assume that it is supported by transonic turbulence ($v_{\text{turb}} \sim c_s$, where v_{turb} is the turbulent velocity, and c_s is the sound speed). The condition of pressure equilibrium then gives the hydrogen density of the coronal gas as

$$n_H = \frac{n_H^{\text{ICM}}}{1 + \gamma/3} \frac{T^{\text{ICM}}}{T}. \quad (14)$$

Numerically, the density is 0.74 cm^{-3} . Then, eqn. (13) yields $f_V \sim 6\text{--}7\%$ for isochoric and isobaric cooling, respectively. Assuming that the coronal gas forms one coherent cylindrical filament, its radius will be $\sqrt{f_V} R$, or $\sim 85\text{--}95 \text{ pc}$. The sound crossing time is $1\text{--}1.2 \text{ Myr}$, while the cooling time is $0.2\text{--}0.3 \text{ Myr}$. In this case too, then, the gas is cooling isochorically. Its mass is now $\sim 5 \times 10^5 M_\odot$, and its entropy is ~ 30 times lower than the cool X-ray gas.

9 DISCUSSION

Our analysis indicates that the coronal gas is a young dynamical feature in NGC 4696. It is unlikely that it has cooled out of the surrounding ICM, or [Fe XIV] would have been observed. Yet, it coincides with the X-ray cool filament in projection, which suggests that the two phases may in fact be co-spatial. The coincidence with the optical filaments is more tenuous and requires further investigation (C11a).

If the optical and coronal phases are not related to each other, the coronal gas could possibly have originated as warm ($\sim 10^4 \text{ K}$) gas that was vigorously heated, and in which cooling has recently been re-established. The energy required to heat the coronal gas from 10^4 K to 10^6 K is $4 \times 10^{53} \text{ erg}$. According to Taylor et al. (2006), the power of the active galactic nucleus (AGN) of NGC 4696 is currently $< 10^{40} \text{ erg s}^{-1}$, which suggests that the AGN outburst lasted at least 1.5 million years. These calculations assume 100% efficiency and do not account for the work required to lift the gas out to 9 kpc, so likely the outburst lasted longer and/or was more powerful. The time-scale is plausible, as it is comparable with the $\sim 2.5 \text{ Myr}$ periodicity of the AGN in M87 (Nulsen et al. 2007). Higher final temperatures ($> 10^6 \text{ K}$) require higher outburst powers, durations, or both. However, this scenario is not satisfactory, because it requires some fine-tuning in order to account for the fact that we get to observe freely cooling gas of such short cooling time.

A more natural explanation would involve the coronal gas as a phase of a steady-state system. Most likely the optical, coronal, and

X-ray phases are related to each other. Then, the coronal gas may be the conductive or mixing interface between the optical, 10^4 K , filaments and the cool X-ray gas, 10^7 K . Examples of conductive interfaces in rough agreement with the coronal gas properties may be found in Boehringer & Fabian (1989). On the other hand, Begelman & Fabian (1990) present crude estimates on the structure of mixing layers. The temperature distribution of the gas in the mixing layer is analytically unknown. The geometric mean temperature is around $300,000 \text{ K}$, subject to unknown, order of unity efficiency factors. This is effectively consistent, to within a factor of a few, with the temperature of the [Fe X] gas. In addition, assuming that the ambient ICM is turbulent, and that the turbulent velocity is close to the sonic speed, we obtain from their equation (2) that the depth of the mixing layer is roughly 1.3 kpc , consistent with the X-ray filament width to a factor of 2. Based on the sharpness of the optical filaments (Crawford et al. 2005), the ICM is thought to not be particularly turbulent, which should improve the agreement with the observations. In fact, plugging in that equation the previous estimate of $\sim 90 \text{ pc}$ for the thickness of the mixing layer, we obtain highly subsonic turbulent motions in the plume, such that $\mathcal{M} < 0.1$.

Note that in the simulations of Esquivel et al. (2006), which do not parametrize uncertainties with efficiency factors, the mixing layer that forms between the 10^4 K and 10^7 K phases has a density-weighted temperature of $1\text{--}2$ million K. However, these simulations do not reach steady-state after 3 Myr of integration, and do not include the effects of NEI. The more recent simulations of Kwak & Shelton (2010) do include non-equilibrium effects, albeit in an idealized two-dimensional, unmagnetized setting. They find that in the simulation most similar to our case (Model F, which has a hot phase temperature of $3 \times 10^6 \text{ K}$) the mixing layer does not reach steady-state by the end of their runs (80 Myr), unlike simulations at lower temperatures for the hot phase. However, they point out that the rate of growth for the mixing layer correlates with the shear speed. This suggests that higher shear speeds may be required to produce a steady-state mixing layer in the X-ray plume.

Signatures of gas at intermediate temperatures may help resolve the state and origin of the coronal gas. Obviously, conduction and mixing models involve multi-temperature gas distributions, so detection of emission lines from intermediate temperature may be expected. Such emission lines have been observed previously in Virgo, where C IV $\lambda 1549$ due to 10^5 K has been reported by Sparks et al. (2009, 2012). Or, in Abell 426, and Abell 1795, where gas at $10^{5.5} \text{ K}$ gives rise to O VI $\lambda\lambda 1032, 1038 \text{ \AA}$ (Bregman et al. 2006). In Figure 8 we present the best candidate lines identified in our cooling simulations. These lines are brighter than the detected [Fe X], also shown. The evolution with time and temperature indicate that some of these lines although very bright are associated with gas of short cooling time, and may not be easily detected. However, if the coronal gas is cooling in a steady state, some of these lines will likely be observable in the ultraviolet.

The non-detection of either [Fe X] or [Fe XIV] in the north west end of the X-ray arc poses difficulties to the mixing and conduction scenarios. The north-west end of the arc lies close to the dust lane, so absorption is a likely cause for the non-detections, without requiring fine tuning of the obscuring column density. Alternatively, or in addition, if that gas lies deeper into the potential well, the mean temperature of the mixing layer may be lower than that at south east end, which would diminish emission from \sim million K gas.

It is also possible that the differences between the two regions are the result of rapid cooling. Non-uniformities in the density field, or in the heating mechanism may accentuate differences in cooling

across the X-ray plume, and lead to a more clumpy gas distribution (as in, e.g., Nulsen 1986). Indeed, the granularity of the sub-keV gas around NGC 4696 (see fig. 1 in C11a) is reminiscent of a collection of clouds.

On the other hand, Panagoulia et al. (2013) reported recently a significant drop in iron abundance within 5–10 kpc of the nucleus in NGC 4696, which is of the order of a few relative to the more remote (say, 20 kpc) ICM. The possibility that the north-west region observed by C11a lies within the depleted region would provide a natural explanation to the absence of any detectable coronal iron emission. It would also require that the X-ray plume is elongated along the line of sight, so that the south-east region lies farther out, and is not drastically affected by the abundance drop.

10 SUMMARY

We have employed self-consistent non-equilibrium cooling calculations implemented in CLOUDY to study the thermal properties of the coronal line gas near the core of NGC 4696. The non-detection of the [Fe XIV] line suggests that the coronal cloud is not a cooling condensation of the surrounding ICM. Fine-tuned values of intrinsic extinction would be required to explain the detection of the optically thin [Fe X], but not of [Fe XIV].

The failure to detect [Fe XIV] suggests a temperature ceiling for the coronal cloud, which we estimate at ~ 2.1 million K. This result is not sensitive to the presence of a temperature floor. The coronal gas is likely embedded in the X-ray plume, but even if it is not, it cools isochorically, and its mass is \sim million M_{\odot} .

Finally, we have briefly explored a few scenarios for the origin of the coronal cloud, and we have pointed out that the cloud is consistent with being either the conductive or the mixing interface between the hot ICM and the warm optical gas. Detailed calculations for observable signatures of these models are beyond the scope of the paper. None the less, we have presented a number of bright lines that trace gas down to 10^4 K.

11 ACKNOWLEDGEMENTS

We would like to thank Orly Gnat & Matthias Steffen for valuable assistance with the validation of the time dependent scheme in CLOUDY. GJF acknowledges support by NSF (0908877; 1108928; and 1109061), NASA (10-ATP10-0053, 10-ADAP10-0073, and NNX12AH73G), JPL (RSA No 1430426), and STScI (HST-AR-12125.01, GO-12560, and HST-GO-12309). ACF thanks European Research Council for the Advanced Grant FEEDBACK. PvH acknowledges support from the Belgian Science Policy Office through the ESA PRODEX program.

REFERENCES

Anders E., Grevesse N., 1989, *Geochim. Cosmochim. Acta*, 53, 197
 Begelman M. C., Fabian A. C., 1990, *MNRAS*, 244, 26P
 Böhringer H., Fabian A. C., 1989, *MNRAS*, 237, 1147
 Bohlin R. C., Savage B. D., Drake J. F., 1978, *ApJ*, 224, 132
 Bregman J. N., Fabian A. C., Miller E. D., Irwin J. A., 2006, *ApJ*, 642, 746
 Canning R. E. A., Fabian A. C., Johnstone R. M., Sanders J. S., Crawford C. S., Ferland G. J., Hatch N. A., 2011, *MNRAS*, 417, 3080 (C11b)

Canning R. E. A., Fabian A. C., Johnstone R. M., Sanders J. S., Crawford C. S., Hatch N. A., Ferland G. J., 2011, *MNRAS*, 411, 411 (C11a)
 Crawford C. S., Hatch N. A., Fabian A. C., Sanders J. S., 2005, *MNRAS*, 363, 216
 Esquivel A., Benjamin R. A., Lazarian A., Cho J., Leitner S. N., 2006, *ApJ*, 648, 1043
 Fabian A. C., 2012, *ARA&A*, 50, 455
 Farage C. L., McGregor P. J., Dopita M. A., Bicknell G. V., 2010, *ApJ*, 724, 267
 Ferland G. J., Porter R. L., van Hoof P. A. M., Williams R. J. R., Abel N. P., Lykins M. L., Shaw G., Henney W. J., Stancil P. C., 2013, *Revista Mexicana de Astronomia y Astrofisica*, 49, 137
 Fitzpatrick E. L., 1999, *PASP*, 111, 63
 Gnat O., Sternberg A., 2007, *ApJS*, 168, 213
 Graham J., Fabian A. C., Sanders J. S., Morris R. G., 2006, *MNRAS*, 368, 1369
 Graney C. M., Sarazin C. L., 1990, *ApJ*, 364, 561 (GS90)
 Henney W. J., Arthur S. J., Williams R. J. R., Ferland G. J., 2005, *ApJ*, 621, 328
 Kwak K., Shelton R. L., 2010, *ApJ*, 719, 523
 Lykins M. L., Ferland G. J., Porter R. L., van Hoof P. A. M., Williams R. J. R., Gnat O., 2013, *MNRAS*, 429, 3133
 McNamara B. R., Nulsen P. E. J., 2007, *ARA&A*, 45, 117
 Meyer J., 1979, in *Liege International Astrophysical Colloquia Vol. 22 of Liege International Astrophysical Colloquia, The significance of the carbonaceous chondrites abundances - Introductory report*. pp 153–187
 Mittal R., O’Dea C. P., Ferland G., Oonk J. B. R., Edge A. C., Canning R. E. A., Russell H., Baum S. A., Böhringer H., Combes F., Donahue M., Fabian A. C., Hatch N. A., Hoffer A., Johnstone R., McNamara B. R., Salomé P., Tremblay G., 2011, *MNRAS*, 418, 2386
 Nulsen P. E. J., 1986, *MNRAS*, 221, 377
 Nulsen P. E. J., Jones C., Forman W. R., David L. P., McNamara B. R., Rafferty D. A., Bîrzan L., Wise M. W., 2007, in Böhringer H., Pratt G. W., Finoguenov A., Schuecker P., eds, *Heating versus Cooling in Galaxies and Clusters of Galaxies AGN Heating Through Cavities and Shocks*. p. 210
 O’Dea C. P., Baum S. A., Maloney P. R., Tacconi L. J., Sparks W. B., 1994, *ApJ*, 422, 467
 Panagoulia E. K., Fabian A. C., Sanders J. S., 2013, *MNRAS*, 433, 3290
 Sanders J. S., Fabian A. C., 2002, *MNRAS*, 331, 273
 Sanders J. S., Fabian A. C., 2006, *MNRAS*, 371, 1483
 Sanders J. S., Fabian A. C., 2011, *MNRAS*, 412, L35
 Sanders J. S., Fabian A. C., Allen S. W., Morris R. G., Graham J., Johnstone R. M., 2008, *MNRAS*, 385, 1186
 Sarazin C. L., Graney C. M., 1991, *ApJ*, 375, 532
 Sparks W. B., Macchetto F., Golombek D., 1989, *ApJ*, 345, 153
 Sparks W. B., Pringle J. E., Carswell R. F., Donahue M., Martin R., Voit M., Cracraft M., Manset N., Hough J. H., 2012, *ApJ*, 750, L5
 Sparks W. B., Pringle J. E., Donahue M., Carswell R., Voit M., Cracraft M., Martin R. G., 2009, *ApJ*, 704, L20
 Taylor G. B., Sanders J. S., Fabian A. C., Allen S. W., 2006, *MNRAS*, 365, 705
 Werner N., Oonk J. B. R., Canning R. E. A., Allen S. W., Simionescu A., Kos J., van Weeren R. J., Edge A. C., Fabian A. C., von der Linden A., Nulsen P. E. J., Reynolds C. S., Ruszkowski M., 2013, *ApJ*, 767, 153

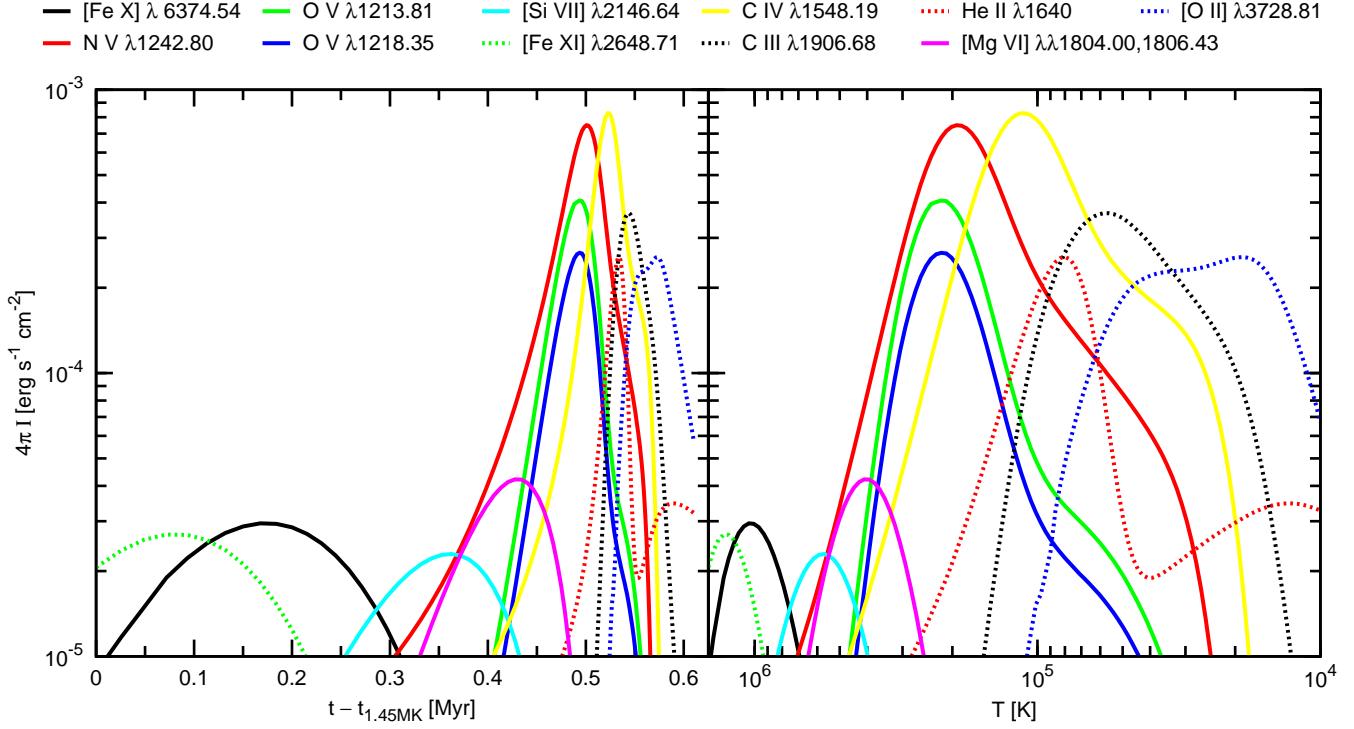


Figure 8. Intensity of various lines produced by a gas column as a function of time (left) and decreasing temperature (right) for our cooling calculations. The column length is equal to the coronal cloud diameter, and the hydrogen density is set to 0.2 cm^{-3} . Time is measured since the moment when the temperature is 1.45 million K.

APPENDIX A: CLOUDY INPUT

As a means to reproduce our results, we provide a minimal input script for isobaric cooling in collisional ionization equilibrium.

```
coronal 8e7 K init time
set dynamics population equilibrium
iterate to convergence
stop time when temperature falls below 1e4 K
c
atom chianti "CloudyChiantiAll.ini"
hden 1 linear
constant gas pressure reset
c
set dr 0
set zone 1
```

This paper has been typeset from a $\text{T}_{\text{E}}\text{X}/\text{L}^{\text{A}}\text{T}_{\text{E}}\text{X}$ file prepared by the author.